Pairing effect on $K^\pi = 0^+$ quadrupole excitations in neutron-rich Mg isotopes studied by Skyrme quasiparticle random-phase approximation calculations in wave-number space

Masayuki Yamagami

Department of Computer Science and Engineering, University of Aizu, Aizu-Wakamatsu, Fukushima 965-8580, Japan

(Received 17 June 2019; revised manuscript received 3 September 2019; published 4 November 2019)

A method of the quasiparticle random-phase approximation (QRPA) calculation using the Skyrme energy density functional (EDF) in three-dimensional wave-number space is presented. This method allows one to perform the QRPA calculation for weakly bound nuclei in much smaller mesh space than that in three-dimensional Cartesian mesh. With this code, I discuss $K^\pi = 0^+$ isoscalar quadruple excitations in neutron-rich Mg isotopes. The large low-lying transition strengths are induced by the strong pairing fluctuation due to the coherent contribution of nonresonant continuum states around the neutron drip line. This could be an experimental probe of novel pairing correlations such as dineutron correlation.

DOI: 10.1103/PhysRevC.100.054302

I. INTRODUCTION

The pairing correlation plays an important role in determining the static and dynamical properties of superfluid nuclei [1,2]. The spatial two-neutron correlation between two weakly bound neutrons, called dineutron correlation, is of special interest, and it has been discussed extensively in the light-mass region, e.g., for ^{11}Li [3–10]. It is argued that the dineutron correlation affects the nature of soft dipole excitation [3–5], and the experimental signatures have been reported [6].

Dineutron correlation is considered to be a universal phenomenon around the neutron drip line. Although the experimental evidence is still under intense debate, it is also suggested in medium- and heavy-mass regions [11–14]. The authors of Ref. [11] emphasized that the pair excitation into continuum states plays a key role in creating the strong spatial correlation, that is also predicted to influence low-lying dipole and octupole excitations in medium-heavy–mass spherical nuclei [11,15].

The two-neutron transfer reaction, that can induce pairing vibration [2], is the more direct probe of pairing correlation. Recently, two-neutron transfer experiments have been conducted in light-mass neutron halo nuclei [16–18]. Theoretical studies for neutron-rich nuclei also have been performed [19–27]. The authors of Refs. [22,27] emphasized that the monopole and quadruple pairing vibrational modes in Sn isotopes are characterized by coherent contributions of nonresonant continuum states, which suggest transfer of a spatially correlated neutron pair.

The pairing vibration might have strong influence on the $K^\pi = 0^+$ isoscalar quadrupole excitation in nuclei with quadruple deformation. The fluctuation of occupation number in Nilsson orbits with different spatial shapes induces the vibration of nucleon density [28]. In our previous studies [29,30], the $K^\pi = 0^+$ excitations were investigated by the quasiparticle random-phase approximation (QRPA) calculation with Woods-Saxon potential in Mg isotopes. However, the role of pair excitation into continuum states was not clear.

In the present study, I demonstrate that the large low-lying transition strengths of the $K^\pi = 0^+$ excitation are induced by the pairing correlation created by coherent contribution of nonresonant continuum states. I perform the QRPA with the Skyrme energy density functional (Skyrme QRPA) for reliable discussion.

The Cartesian (**r**-space) mesh is often used for descriptions of deformations and weakly binding and continuum effects in unstable nuclei [31]. The Skyrme QRPA calculation in axially symmetric **r**-space mesh was done in Refs. [32–35]. By solving the QRPA problem iteratively (the finite amplitude method) [36], the authors of Ref. [37] performed the Skyrme QRPA calculation in the three-dimensional **r**-space mesh. Recently, the pygmy dipole modes in ^{40}Mg were investigated by performing the Skyrme QRPA in axially symmetric **r**-space mesh [38]. The large box size 27.6 fm is used for description of the particle-hole (ph) excitations from weakly bound to continuum states.

I perform the QRPA calculation in three-dimensional wave-number space (**k**-space) mesh. The wave functions with spatially extended structure can be best studied in **k**-space, where the wide spatial distributions in **r**-space translates into a narrow distribution in **k**-space [39]. Moreover multipole operators with the radial dependence r^L (r^2 for $L = 0$) are decreasing functions of $|\mathbf{k}|$ in **k**-space. Eventually, the dominant contribution to the ph-type matrix element comes from the low-$|\mathbf{k}|$ region. This advantage allows us to perform the Skyrme QRPA calculation in much smaller mesh space than that in **r**-space mesh.

This paper is organized as follows. In Sec. II, I explain the Hartree-Fock-Bogoliubov (HFB) method in **k**-space mesh. In Sec. III, I show the features of QRPA in **k**-space mesh. In Sec. IV, I discuss the ground state properties of neutron-rich Mg isotopes. The continuum effect for pairing correlation is a focus. In Sec. V, I clarify the influence of the pairing

correlation on the low-lying transition strengths of the $K^\pi = 0^+$ isoscalar quadrupole excitations in Mg isotopes. The conclusion is drawn in Sec. VI. The convergence of the QRPA calculation is checked in the Appendix.

II. HFB IN WAVE NUMBER SPACE

A. Symmetries

I solve the QRPA equation in the matrix form using the canonical single-particle state [1,40]. First, the HFB equation

$$\begin{pmatrix} h'-\lambda & \Delta \\ -\Delta^* & -h'+\lambda \end{pmatrix}\begin{pmatrix} U_k \\ V_k \end{pmatrix} = E_k \begin{pmatrix} U_k \\ V_k \end{pmatrix} \tag{1}$$

is solved in the Hartree-Fock (HF) basis φ_l satisfying $h'\varphi_l = \varepsilon_l\varphi_l$ (the two-basis method [41]). Here, the λ is a chemical potential, and the index l runs over integers which distinguish the single-particle states. I consider pairing correlation between like particles, and the index for distinguishing proton and neutron is omitted if it is obvious.

The single-particle Hamiltonian $h' = h - \omega_{\rm rot} j_x$ describes the independent-particle motion in a uniformly rotating triaxially deformed potential. The Skyrme energy density functional (EDF) is used for h, and the j_x is the single-particle angular momentum operator. The rotational frequency is set to $\omega_{\rm rot} = 0$ in this study, although the time-reversal symmetry is not imposed on φ_l for future studies.

Two discrete symmetries, the parity $\mathcal{P}$ and the rotation about the x axis by the angle of π, $\mathcal{R}_x = e^{i\pi j_x/\hbar}$, are imposed on the single-particle wave functions

$$\varphi_l^{(\wp_l,\alpha_l)}(\mathbf{r}) = \begin{pmatrix} \Phi_l^{(\wp_l,\alpha_l)}(\mathbf{r},+1) \\ \Phi_l^{(\wp_l,\alpha_l)}(\mathbf{r},-1) \end{pmatrix}. \tag{2}$$

The $\Phi_l^{(\wp_l,\alpha_l)}(\mathbf{r},\sigma)$ denotes the component of the single-particle wave function with spin $\frac{1}{2}\sigma$ ($\sigma = \pm 1$) along the z direction. The $\wp_k$ ($= \pm 1$) and α_k ($= \pm i$) are called parity and x signature, and they satisfy $\mathcal{P}\varphi_l^{(\wp_l,\alpha_l)}(\mathbf{r}) = \wp_l\varphi_l^{(\wp_l,\alpha_l)}(\mathbf{r})$ and $\mathcal{R}_x\varphi_l^{(\wp_l,\alpha_l)}(\mathbf{r}) = \alpha_l\varphi_l^{(\wp_l,\alpha_l)}(\mathbf{r})$ [31,42]. The indexes $\wp_l$ and α_l are often neglected if it is obvious.

The $\mathcal{P}$ and $\mathcal{R}_x$ symmetries allow us to represent $\varphi_l^{(\wp_l,\alpha_l)}(\mathbf{r})$ by linear combination of real functions $\phi_{\alpha_l,l}^{(\pi_x,\pi_y,\pi_z)}(\mathbf{r})$ [31,43,44],

$$\begin{aligned}\varphi_l^{(+1,+i)}(\mathbf{r}) &= \left[\phi_{+i,l}^{(+,+,+)}(\mathbf{r}) + i\phi_{+i,l}^{(+,-,-)}(\mathbf{r})\right]\mathbf{e}_1 \\ &\quad + \left[\phi_{+i,l}^{(-,-,+)}(\mathbf{r}) + i\phi_{+i,l}^{(-,+,-)}(\mathbf{r})\right]\mathbf{e}_2, \qquad (3)\\ \varphi_l^{(+1,-i)}(\mathbf{r}) &= \left[\phi_{-i,l}^{(-,-,+)}(\mathbf{r}) + i\phi_{-i,l}^{(-,+,-)}(\mathbf{r})\right]\mathbf{e}_1 \\ &\quad + \left[\phi_{-i,l}^{(+,+,+)}(\mathbf{r}) + i\phi_{-i,l}^{(+,-,-)}(\mathbf{r})\right]\mathbf{e}_2, \qquad (4)\\ \varphi_l^{(-1,+i)}(\mathbf{r}) &= \left[\phi_{+i,l}^{(-,+,+)}(\mathbf{r}) + i\phi_{+i,l}^{(-,-,-)}(\mathbf{r})\right]\mathbf{e}_1 \\ &\quad + \left[\phi_{+i,l}^{(+,-,+)}(\mathbf{r}) + i\phi_{+i,l}^{(+,+,-)}(\mathbf{r})\right]\mathbf{e}_2, \qquad (5)\\ \varphi_l^{(-1,-i)}(\mathbf{r}) &= \left[\phi_{-i,l}^{(+,-,+)}(\mathbf{r}) + i\phi_{-i,l}^{(+,+,-)}(\mathbf{r})\right]\mathbf{e}_1 \\ &\quad + \left[\phi_{-i,l}^{(-,+,+)}(\mathbf{r}) + i\phi_{-i,l}^{(-,-,-)}(\mathbf{r})\right]\mathbf{e}_2. \qquad (6)\end{aligned}$$

The $\phi_{\alpha_l,l}^{(\pi_x,\pi_y,\pi_z)}(\mathbf{r})$ have reflection symmetry with respect to $x = 0$, $y = 0$, and $z = 0$ planes such as $\phi_{\alpha_l,l}^{(\pm,\pi_y,\pi_z)}(-x,y,z) = \pm\phi_{\alpha_l,l}^{(\pm,\pi_y,\pi_z)}(x,y,z)$. The vectors in spin-$\frac{1}{2}$ space, $\mathbf{e}_1 = \frac{1}{\sqrt{2}}(1,1)^T$ and $\mathbf{e}_2 = \frac{1}{\sqrt{2}}(1,-1)^T$, are used.

B. Wave-number space mesh

The real functions $\phi_{\alpha_l,l}^{(\pi_x,\pi_y,\pi_z)}(\mathbf{r})$ are represented by the Fourier-series expansion method:

$$\phi_{\alpha_l,l}^{(\pi_x,\pi_y,\pi_z)}(\mathbf{r}) = \sum_{\mathbf{n}}^{N_{\rm max}} \phi_{\alpha_l,l,\mathbf{n}}^{(\pi_x,\pi_y,\pi_z)} f_{n_x}^{(\pi_x)}(x) f_{n_y}^{(\pi_y)}(y) f_{n_z}^{(\pi_z)}(z). \tag{7}$$

Here, $\phi_{\alpha_l,l,\mathbf{n}}^{(\pi_x,\pi_y,\pi_z)}$ are wave functions in $\mathbf{k}$-space mesh. The summation of $\mathbf{n} = (n_x,n_y,n_z)$ runs over non-negative integers n_x, n_y, and n_z satisfying $n_x + n_y + n_z \leqslant N_{\rm max}$.

The function $f_n^{(\pi)}(x)$ is defined in the interval $-R_{\rm b} \leqslant x \leqslant R_{\rm b}$ and has a definite parity: $f_n^{(\pm)}(-x) = \pm f_n^{(\pm)}(x)$. The explicit form is

$$f_n^{(+)}(x) = \frac{1}{\sqrt{(1+\delta_{0,n})R_{\rm b}}}\cos k_n x, \tag{8}$$

$$f_n^{(-)}(x) = \frac{1}{\sqrt{R_{\rm b}}}\sin k_n x \tag{9}$$

with $k_n = n\Delta k$. The $\mathbf{k}$-space mesh is discretized as $\mathbf{k_n} = (n_x\Delta k, n_y\Delta k, n_z\Delta k)$. The $\Delta k = \pi/R_{\rm b}$ and $k_{\rm max} = N_{\rm max}\Delta k$ define the spacing and size of the $\mathbf{k}$-space mesh. The parameters $N_{\rm max} = 12$ and $\Delta k = 0.38$ fm^{-1} for $k_{\rm max} = 4.56$ fm^{-1} are adopted in our calculation (see Appendix for the details).

C. Pairing interaction

The density-dependent zero-range interaction

$$V_{\rm pair}(\mathbf{r},\mathbf{r}') = \frac{1}{2}V_0(1-P_\sigma)\left[1-\eta_0\frac{\rho(\mathbf{r})}{\rho_0}\right]\delta(\mathbf{r}-\mathbf{r}') \tag{10}$$

is widely used in density functional theory calculations [45,46] and three-body calculations [3,4,47]. Here, V_0 is the interaction strength, P_σ is the spin-exchange operator, and $\rho_0 = 0.16$ fm^{-3}. The pairing forces with $\eta_0 = 0$, 1/2, and 1 are called volume type, mixed type, and surface type respectively [48,49].

The zero-range interactions lead to divergences and can be meaningful as effective interactions within a truncated space of states. In Refs. [3,47,50], it was proposed that the interaction strength V_0 should be deduced from the low-energy s-wave phase shift δ of neutron-neutron (nn) scattering. The scattering problem in free space with the pairing interaction (10) can be exactly solved with the states truncated by a wave-number space cutoff $k \leqslant k_c$,

$$k\cot\delta = -\frac{1}{a_{nn}} - \frac{k}{\pi}\ln\frac{k_c-k}{k_c+k}. \tag{11}$$

Here, a_{nn} is the scattering length and one can derive an expression for the effective range $r_{nn} = 4/(\pi k_c)$ and the cutoff energy [47,51]

$$e_{\rm cut} = \frac{\hbar^2k_c^2}{2m} = \frac{\hbar^2}{2m}\left[\frac{4}{\pi r_{nn}}\right]^2. \tag{12}$$

The cutoff energy for the center-of-mass frame used in Refs. [3,47,50] is defined by $e_{\rm cut}^{\rm (cm)} = 2e_{\rm cut}$. The interaction strength V_0 is expressed by [47]

$$V_0 = -\frac{2\pi^2\hbar^2 m^{-1}}{k_c - \pi/(2a_{nn})}. \tag{13}$$

It is considered that for a given cutoff energy $e_{\rm cut}$ the scattering length a_{nn} is an adjustable parameter for the low wave number k region of the phase shift [47,50], because the empirical values $a_{nn} = -18.5$ fm and $r_{nn} = 2.8$ fm ($e_{\rm cut} = 4.3$ MeV) cannot well reproduce the wave number k dependence of the phase shift δ obtained by using realistic nn interactions. The optimal parameter a_{nn} can be found for cutoff energies satisfying $7.5 \lesssim e_{\rm cut} \lesssim 10$ MeV. Although the medium effects in nuclei modify the effective interaction and generate density dependent terms, the cutoff energy should not be far away from $e_{\rm cut} = 10$ MeV for consistency with the low-energy nn scattering.

In the configurational HFB calculations, the pairing problem is considered in the energy window defined by $|\varepsilon_l - \lambda| < E_{\rm pair}$. The cutoff energy $E_{\rm pair}$ can be compared with the quasiparticle energy cutoff $E_l < E_{\rm pair}$ (E_l is the quasiparticle energy of the single-particle state l), and can be related to the cutoff $e_{\rm cut}$ in free space by $E_{\rm pair} = e_{\rm cut}$ [50,51].

In the present study, the pairing correlation is active for single-particle states satisfying

$$-E_{\rm pair}^{(-)} < \varepsilon_l - \lambda < E_{\rm pair}^{(+)}.$$

The lower cutoff $E_{\rm pair}^{(-)} = 10$ MeV is fixed. The upper cutoff $E_{\rm pair}^{(+)}$ is varied in order to examine the influence of continuum single-particle states. It will be shown that the HFB and QRPA calculations converge by using the upper cutoff $E_{\rm pair}^{(+)} = 10$ MeV (see Secs. IV B and V D for details).

The density dependence parameter η_0 is determined in order to produce the known ground-state properties. In Refs. [4,47], it was shown that the three-body calculations using the density dependence parameter $\eta_0 = 1$ and the interaction strength V_0 of Eq. (13) with the scattering length $a_{nn} = -15$ fm well describe the ground-state properties in light-mass halo nuclei.

The optimization for the interaction strength V_0 and the density dependence parameter η_0 in the HFB calculation with the Skyrme EDFs show that the parameter $\eta_0 = 0.875$, that is close to the surface type, minimizes the root-mean-square deviation between the experimental and theoretical neutron pairing gaps in even-even nuclei across the nuclear chart, as shown in Fig. 5 of Ref. [52].

From these considerations, I mainly use the surface-type pairing force. I also examine the mixed- and volume-type pairing forces for comparison of how the discussion depends on the choice, because the form of pairing energy density functional and the choice of the parameters are still under discussion [50–53]. The interaction strength V_0 is fixed by the neutron paring gap in ^{34}Mg for each set of three elements: the cutoff energy $E_{\rm pair}^{(+)}$, the density dependence parameter η_0, and the Skyrme EDF (see Sec. IV A for the details).

D. Canonical state

The density matrix and pairing tensor [1,40] are defined by

$$\rho_{ll'} = \langle\Psi|c_{l'}^\dagger c_l|\Psi\rangle\,, \tag{14}$$

$$\kappa_{ll'} = \langle\Psi|c_l c_{l'}|\Psi\rangle\,, \tag{15}$$

where $c_l^\dagger$ and c_l are the particle operators of the HF state and $|\Psi\rangle$ is the quasiparticle vacuum. The ρ is diagonal in the canonical state: $\rho_{{\rm can},kk'} = v_k^2\delta_{kk'}$. The eigenvalues of ρ are the occupation probabilities v_k^2 and the eigenvectors are the coefficients D_{lk} of the unitary transformation from $c_l^\dagger$ to the canonical state $a_k^\dagger$:

$$a_k^\dagger = \sum_l D_{lk} c_l^\dagger. \tag{16}$$

The canonical single-particle wave functions $\varphi_{{\rm can},k}$ are also constructed in the same way. The $\varphi_{{\rm can},k}$ with $v_k^2 > 0$ is a localized function in $\mathbf{r}$ space even for the canonical single-particle energy $\varepsilon_{{\rm can},k} = \langle\varphi_{{\rm can},k}|h|\varphi_{{\rm can},k}\rangle > 0$ [54–56].

The $|\Psi\rangle$ has the BCS form

$$|\Psi\rangle = \prod_{k>0}(u_k + v_k a_k^\dagger a_{\bar{k}}^\dagger)\,|-\rangle\,. \tag{17}$$

The product runs only the positive-signature state, that is expressed as $k > 0$. For each $k > 0$, there exists a conjugate state $\bar{k} < 0$ that has negative signature. The phase convention $u_{\bar{k}} = u_k > 0$, $v_{\bar{k}} = -v_k < 0$ is adopted. The quasiparticle operators are defined by

$$\alpha_k^\dagger = u_k a_k^\dagger - v_k a_{\bar{k}}, \tag{18}$$

$$\alpha_{\bar{k}}^\dagger = u_k a_{\bar{k}}^\dagger + v_k a_k, \tag{19}$$

and the κ in the canonical form is $\kappa_{k\bar{k}'} = u_k v_{k'}\delta_{kk'}$ [40]. The quasiparticle energy is defined by

$$E_k = \sqrt{(\varepsilon_{{\rm can},k} - \lambda)^2 + \left(\Delta_{k\bar{k}}^{\rm (can)}\right)^2} \tag{20}$$

with the pairing gap in the canonical basis

$$\Delta_{k\bar{k}}^{\rm (can)} = \frac{1}{2}\sum_l \langle k\bar{k}|V_{\rm pair}|l\bar{l}\rangle\, u_l v_l. \tag{21}$$

For comparison to the experimental pairing gap, the averaged pairing gap [57,58] is defined by

$$\bar{\Delta} = \sum_{k>0} u_k v_k \Delta_{k\bar{k}}^{\rm (can)} \Big/ \sum_{k>0} u_k v_k. \tag{22}$$

III. QRPA CALCULATION

A. QRPA equation

The wave functions of the QRPA excitation are a superposition of

$$\Psi_{kk'}^{(\wp,\xi)}(\mathbf{r}) = \left[\varphi_{{\rm can},k}^{(\wp_k,\alpha_k)}(\mathbf{r})\right]^\dagger \varphi_{{\rm can},k'}^{(\wp_{k'},\alpha_{k'})}(\mathbf{r}). \tag{23}$$

They can be classified by the parity $\wp = \wp_k\wp_{k'} = \pm 1$ and the x signature $\xi = (\alpha_k)^*\alpha_{k'} = \pm 1$. The QRPA equation is

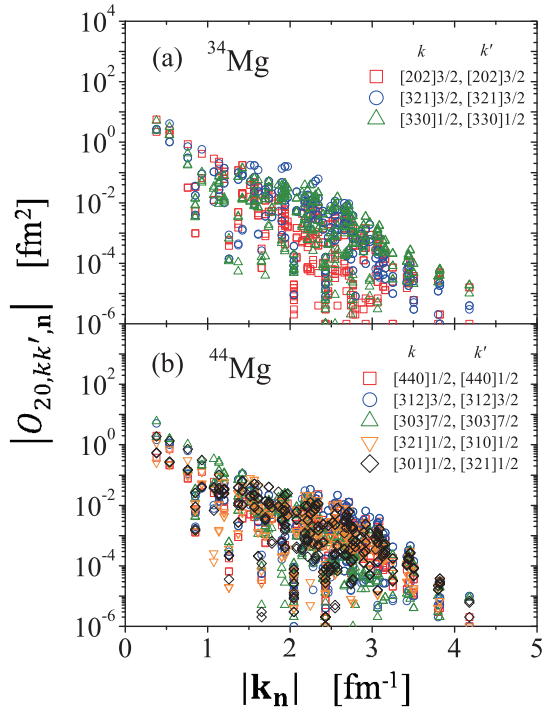

FIG. 1. One-body matrix elements $O_{20,kk',\mathbf{n}}$ in **k**-space mesh are shown as a function of $|\mathbf{k_n}|$. Panel (a) is for the main neutron two-quasiparticle configurations of the lowest $K^\pi = 0^+$ state in ^{34}Mg and (b) is the same but for ^{44}Mg. The SkM* and the surface-type pairing force are used. See text for the details.

separated into sectors of $(\wp, \xi)$,

$$\sum_{jj'} \begin{pmatrix} A^{(\wp,\xi)}_{kk'jj'} & B^{(\wp,\xi)}_{kk'jj'} \\ -B^{(\wp,\xi)*}_{kk'jj'} & -A^{(\wp,\xi)*}_{kk'jj'} \end{pmatrix} \begin{pmatrix} f^{(\wp,\xi)}_{\nu,jj'} \\ g^{(\wp,\xi)}_{\nu,jj'} \end{pmatrix} = E^{(\wp,\xi)}_\nu \begin{pmatrix} f^{(\wp,\xi)}_{\nu,kk'} \\ g^{(\wp,\xi)}_{\nu,kk'} \end{pmatrix}. \quad (24)$$

The cutoff energy is imposed on the two-quasiparticle energy $E_k + E_{k'} < 30$ MeV.

The one-body transition operators $O^{(\xi)}_{LK}$ can be classified by the z component K of its angular momentum and the x signature $\xi = \pm 1$ representing the symmetry property for rotation about the x axis: $\mathcal{R}_x O^{(\xi)}_{LK} \mathcal{R}_x^{-1} = \xi O^{(\xi)}_{LK}$ [42,59].

In this paper, I concentrate on the $(\wp, \xi) = (+1, +1)$ sector containing $(L, K) = (2, 0)$ and $(2, -1)$ modes [59]. The indexes $\wp$ and ξ are often neglected if it is obvious. The explicit forms of the transition operators are $O_{20} = r^2 Y_{20} = \sqrt{\frac{5}{16\pi}}(2z^2 - x^2 - y^2)$ and $O_{2,-1} = \frac{i}{\sqrt{2}} r^2 [Y_{2,-1} + Y_{2,1}] = \sqrt{\frac{15}{4\pi}} yz$ in terms of the spherical harmonics function Y_{LK}.

The real and imaginary parts of $\Psi_{kk'}(\mathbf{r})$ with $(\wp, \xi) = (+1, +1)$ can be written as

$$\mathrm{Re}[\Psi_{kk'}(\mathbf{r})] = \sum_{\mathbf{n}} \Psi^{(R)}_{kk',\mathbf{n}} f^{(+1)}_{n_x}(x) f^{(+1)}_{n_y}(y) f^{(+1)}_{n_z}(z),$$

$$\mathrm{Im}[\Psi_{kk'}(\mathbf{r})] = \sum_{\mathbf{n}} \Psi^{(I)}_{kk',\mathbf{n}} f^{(+1)}_{n_x}(x) f^{(-1)}_{n_y}(y) f^{(-1)}_{n_z}(z). \quad (25)$$

Here, $\Psi^{(R)}_{kk',\mathbf{n}}$ and $\Psi^{(I)}_{kk',\mathbf{n}}$ are wave functions in **k**-space mesh, and they are real numbers.

B. One-body matrix element

The one-body matrix element

$$O_{LK,kk'} = \int_{-R_b}^{R_b} \int_{-R_b}^{R_b} \int_{-R_b}^{R_b} O_{LK}(\mathbf{r}) \Psi_{kk'}(\mathbf{r}) dx\, dy\, dz \quad (26)$$

can be expressed in **k**-space mesh by

$$O_{20,kk'} = \sum_{\mathbf{n}} O_{20,kk',\mathbf{n}}, \quad (27)$$

$$O_{2,-1,kk'} = \sum_{\mathbf{n}} O_{2,-1,kk',\mathbf{n}} \quad (28)$$

with

$$O_{20,kk',\mathbf{n}} = \Psi^{(R)}_{kk',\mathbf{n}} \big(2\delta_{n_x,0}\delta_{n_y,0}\hat{O}_{20,n_z} - \delta_{n_y,0}\delta_{n_z,0}\hat{O}_{20,n_x} - \delta_{n_x,0}\delta_{n_z,0}\hat{O}_{20,n_y}\big), \quad (29)$$

$$O_{2,-1,kk',\mathbf{n}} = \Psi^{(I)}_{kk',\mathbf{n}} \delta_{n_x,0} \hat{O}_{2,-1,n_y,n_z}. \quad (30)$$

Here, $\hat{O}_{2,n}$ and $\hat{O}_{2,-1,nn'}$ are defined by $\hat{O}_{20,0} = \sqrt{5/(18\pi)} R_b^{7/2}$,

$$\hat{O}_{20,n} = \sqrt{\frac{5}{16\pi}} (\sqrt{2R_b})^2 \int_{-R_b}^{R_b} x^2 f^{(+)}_n(x) dx = (-1)^n \sqrt{\frac{20}{\pi}} \frac{R_b^{3/2}}{k_n^2}, \quad (31)$$

$$\hat{O}_{2,-1,nn'} = \sqrt{\frac{15}{4\pi}} \sqrt{2R_b} \int_{-R_b}^{R_b} \int_{-R_b}^{R_b} yz f^{(-)}_n(y) f^{(-)}_{n'}(z) dy\, dz = (-1)^{n+n'} 2 \sqrt{\frac{30}{\pi}} \frac{R_b^{3/2}}{k_n k_{n'}} \quad (32)$$

for $n, n' \geqslant 1$.

The $\hat{O}_{20,n}$ and $\hat{O}_{2,-1,nn'}$ are decreasing functions of $|\mathbf{k_n}|$, and the canonical single-particle wave functions $\varphi_{\mathrm{can},k}$ with $v_k^2 > 0$ are localized in the low-$|\mathbf{k_n}|$ region (see discussion in Sec. II D). Eventually, the dominant contribution to ph-type matrix elements, Eqs. (27) and (28), comes from the low-$|\mathbf{k_n}|$ components.

Figures 1(a) and 1(b) display the $O_{20,kk',\mathbf{n}}$ of the main two-quasiparticle configurations of the lowest $K^\pi = 0^+$ states in ^{34}Mg and ^{40}Mg as a function of $|\mathbf{k_n}|$ (see Sec. V for details of the configurations). Actually, the large components appear in the low-$|\mathbf{k_n}|$ region, and the $|O_{20,kk',\mathbf{n}}|$ decrease exponentially as a function of $|\mathbf{k_n}|$. The same description can hold for any multipole operators of the radial dependence r^L (r^2 for $L = 0$). This is a strong advantage of the **k**-space mesh.

The situation is different in **r**-space mesh. The integrand $O_{KL}(\mathbf{r})\Psi_{kk'}(\mathbf{r})$ in Eq. (26) has a peak around or outside of the nuclear surface. Especially the significant contribution to $O_{LK,kk'}$ comes from the far outside region (typically, $r \geqslant 20$ fm) when halo-type single-particle states are involved [60]. Therefore, for the accurate description of wave functions in the low density asymptotic region it is essential to use large box size or the exact treatment of the asymptotic form in the HFB approach for deformed nuclei [61].

C. Transition strength

The νth QRPA excited state is expressed as $|\nu\rangle = Q_\nu^\dagger|0\rangle$ with excitation operator

$$Q_\nu^\dagger = \sum_{kk'} f_{\nu,kk'}\alpha_k^\dagger\alpha_{k'}^\dagger - g_{\nu,kk'}\alpha_{k'}\alpha_k. \quad (33)$$

For the ph-type one-body operator

$$O_{LK}^{(\mathrm{ph})} = \sum_{kk'} O_{LK,kk'}a_k^\dagger a_{k'}, \quad (34)$$

the transition matrix element between $|\nu\rangle$ and the ground state $|0\rangle$ is expressed as

$$M_{LK}^{(\mathrm{ph,ch})}(\nu) = \langle\nu\,|\,O_{LK}^{(\mathrm{ph})}\,|\,0\rangle \equiv \sum_{kk'} M_{LK,kk'}^{(\mathrm{ph})}(\nu). \quad (35)$$

The summation over (k, k') runs over both neutron and proton two-quasiparticle configurations for the isoscalar transition matrix element $M_{LK}^{(\mathrm{ph,IS})}(\nu)$. The neutron transition matrix element is defined by

$$M_{LK}^{(\mathrm{ph},n)}(\nu) = M_{LK}^{(\mathrm{ph},n(\mathrm{pair}))}(\nu) + M_{LK}^{(\mathrm{ph},n(\mathrm{no\ pair}))}(\nu), \quad (36)$$

where the partial sum is restricted to the neutron pairing channel $(k = k')$ for $M_{LK}^{(\mathrm{ph},n(\mathrm{pair}))}(\nu)$ and to the neutron ph channel $(k \neq k')$ for $M_{LK}^{(\mathrm{ph},n(\mathrm{no\ pair}))}(\nu)$. The proton transition matrix element $M_{LK}^{(\mathrm{ph},p)}(\nu)$ is also defined.

The isoscalar transition strength is defined by $B(Q^{\mathrm{IS}}2;\nu) = |M_{20}^{(\mathrm{ph,IS})}(\nu)|^2$. The neutron and proton transition strengths $B(Q^n2;\nu)$ and $B(E2;\nu)$ are also defined in the same way.

The partial sum of transition matrix elements up to cutoff energy $E_{2\mathrm{qp}}^{(\mathrm{cut})}$ is defined by

$$M_{KL}^{(\mathrm{ph,ch})}\left(\nu; E_{2\mathrm{qp}}^{(\mathrm{cut})}\right) = \sum_{E_k + E_{k'} < E_{2\mathrm{qp}}^{(\mathrm{cut})}} M_{KL,kk'}^{(\mathrm{ph})}(\nu). \quad (37)$$

The particle-particle (pp) type matrix element is also expressed as

$$M_{LK}^{(\mathrm{pp})}(\nu) = \langle\nu\,|\,O_{LK}^{(\mathrm{pp})}\,|\,0\rangle \equiv \sum_{k>0} M_{LK,kk}^{(\mathrm{pp})}(\nu) \quad (38)$$

with

$$O_{LK}^{(\mathrm{pp})} = \sum_{k>0} O_{LK,kk}a_k^\dagger a_{\bar{k}}^\dagger. \quad (39)$$

The index ν in matrix elements is often neglected if it is obvious.

D. Residual interaction

The ph residual interaction is derived from the Skyrme EDF through the Landau-Migdal approximation [62–64]:

$$V_{\mathrm{ph}}(\mathbf{r},\mathbf{r}') = N_0^{-1}[F_0 + F_0'\tau\cdot\tau' + (G_0 + G_0'\tau\cdot\tau')\sigma\cdot\sigma']\delta(\mathbf{r}-\mathbf{r}'). \quad (40)$$

For the pairing channel, I use the same pairing force V_{pair} of Eq. (10).

If the same Hamiltonian is consistently used in both HFB and QRPA, and the model space is enough large, the spurious modes appear at zero energy and they are decoupled from other eigenmodes of QRPA. However the Landau-Migdal approximation is used for the ph residual interaction, and the cutoff energies for the pairing-active space and the two-quasiparticle configuration are imposed due to the excessive demand on computer resources. Therefore the V_{ph} and V_{pair} are normalized by multiplying factors f_{ph} and f_{pp} ($V_{\mathrm{ph}} \to f_{\mathrm{ph}}V_{\mathrm{ph}}$, $V_{\mathrm{pair}} \to f_{\mathrm{pp}}V_{\mathrm{pair}}$) to obtain zero energies of the spurious rotational mode with $(L, K) = (2, -1)$ and the spurious particle number fluctuation mode with $(L, K) = (0, 0)$. The technical details can be found in Refs. [30,32].

IV. GROUND STATE PROPERTIES

A. Neutron drip line and deformation

The quadrupole deformation in neutron-rich Mg isotopes has been of interest in determining how the region of deformation expands from the quenched spherical magic number $N = 20$. Recent observations of the energy ratio of the first and second excited states in ^{34,36,38}Mg revealed the quadrupole deformation [65–67]. The low excitation energy in ^{40}Mg suggests the quenching of spherical magic number $N = 28$ and the prolately deformed ground states [68]. Theoretical studies also have predicted the prolate deformation in ^{34,36,38,40}Mg (for example, see Refs. [69–75]).

The prediction of the two-neutron drip line depends on the models: for example, ^{40}Mg in the macroscopic-microscopic model [74], the antisymmetrized molecular dynamics method [72], and the HFB with Skyrme SLy4 [75], Gogny D1S [69], and M3Y-P6 [70]. It is also predicted that the two-neutron drip line nucleus is ^{42}Mg in the relativistic Hartree Bogoliubov (RHB) model with PK1 [73], and ^{46}Mg in the HFB with Skyrme BSk24 [71] and the RHB with NL3 [73].

I adopt the Skyrme SkM* [76] and UNEDF0 [77] EDFs. The SkM* is one of the standard EDFs, that well describes deformation properties. The UNEDF0 is a result of state-of-the-art optimization. The pairing strength V_0 is fitted to the neutron pairing gap Δ_n in ^{34}Mg. Here, the experimental pairing gap is extracted by the three-point odd-even staggering of nuclear masses [78]. The proton pairing is not considered in the current study, because the proton pairing gaps are negligible in neutron-rich Mg isotopes when the density-dependent pairing force is used [53].

The predicted two-neutron drip line nucleus is ^{44}Mg and the neutron chemical potential is $\lambda_n = -0.173$ MeV in the calculation using the SkM*, while ^{42}Mg and $\lambda_n = -0.156$ MeV in the calculation using the UNEDF0. Here the surface-type pairing force with $E_{\mathrm{pair}}^{(+)} = 10$ MeV is used. Figure 2 shows the quadrupole deformation parameter β_2 obtained with the SkM* and UNEDF0. Here, the triaxial deformation parameter γ is negligible in these nuclei.

Figure 3 displays the canonical single-particle energies in ^{34,40,44}Mg obtained with the SkM*. The red (blue) line represents the positive- (negative-) parity single-particle level. The solid (dashed) line indicates the single-particle level that has prolate (oblate) density distribution with $\beta_k = \langle\varphi_{\mathrm{can},k}|r^2Y_{20}|\varphi_{\mathrm{can},k}\rangle > 0$ (<0). The thin dotted line represents the discretized nonresonant continuum states. The nonresonant continuum states are identified by checking the Δk dependence (equivalent to the box size R_b dependence) of the single-particle energies [45].

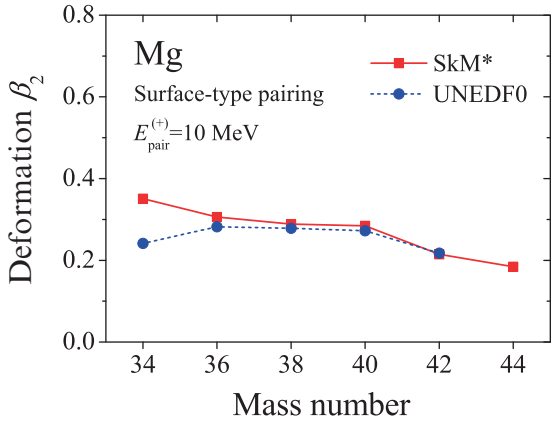

FIG. 2. Quadrupole deformation parameter β_2 in neutron-rich Mg isotopes. The results using the SkM* and UNEDF0 are shown. The surface-type pairing force with $E^{(+)}_{\rm pair} = 10$ MeV is used.

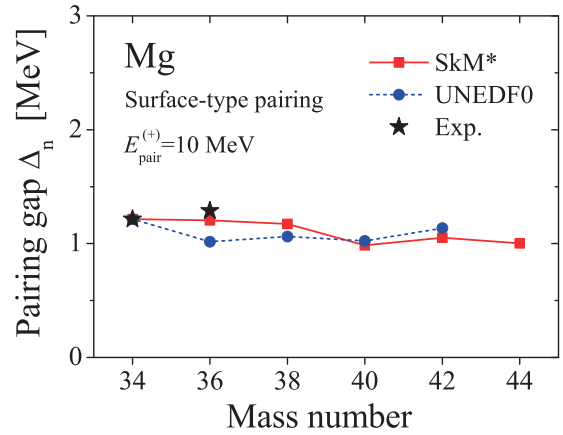

FIG. 4. Same as Fig. 2 but for the neutron pairing gap Δ_n. The experimental data are also shown. The pairing strength parameter V_0 is fixed at ^{34}Mg.

B. Continuum effect for pairing

Figure 4 shows the neutron pairing gaps Δ_n in neutron-rich Mg isotopes. The results with the SkM* and UNEDF0 are compared. The surface-type pairing force is used in both calculations. One finds that the neutron pairing gaps Δ_n are almost constant from ^{34}Mg to the neutron drip line in both calculations.

In order to clarify the role of continuum states in pairing correlations, the cutoff energy $E^{(+)}_{\rm pair}$ dependence is examined in Fig. 5. Here, the SkM* and the surface-type pairing force are used. With $E^{(+)}_{\rm pair} = 5$ MeV, which is a typical model size for stable nuclei [31], the neutron pairing gap Δ_n gradually decreases as a function of mass number. The quenching at ^{40}Mg with small $E^{(+)}_{\rm pair}$ is due to missing resonant single-particle states at $\varepsilon_{{\rm can},k} \approx 6$ MeV.

The contribution of continuum states up to $E^{(+)}_{\rm pair} = 10$ MeV becomes sizable around the neutron drip line. The cutoff energy $E^{(+)}_{\rm pair} = 10$ MeV is consistent with the low-energy nn scattering, and reasonable for the description of the pairing correlation in weakly bound nuclei (see Sec. II C for the details).

I note that the single-particle state with $\varepsilon = (\hbar k_{\rm c})^2/2m \approx 10$ MeV has a cutoff wave number $k_{\rm c} \approx 0.27$ fm^{-1}. The spatial size $\Delta x \approx 1/k_{\rm c} \approx 3.7$ fm is comparable to the predicted diameter of a dineutron in ^{40}Mg [53], in light-mass neutron halo nuclei [79], and in medium-heavy neutron-rich nuclei [11].

The authors of Ref. [11] emphasized that the coherent contribution of the nonresonant continuum states with high-orbital angular momentum l is involved to produce the dineutron correlation in spherical neutron-rich nuclei. A two-particle wave function made of the relative s wave brings

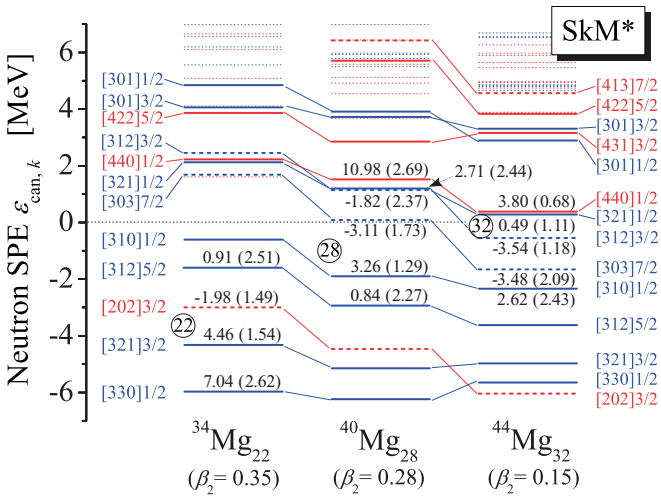

FIG. 3. Neutron canonical single-particle energies in ^{34,40,44}Mg. The blue (red) line represents the negative (positive) parity level. The solid (dashed) line indicates the level with prolate (oblate) density distribution. The thin dotted line represents discretized nonresonant continuum states. The quadruple matrix element $\beta_k = \langle\varphi_{{\rm can},k}|r^2Y_{20}|\varphi_{{\rm can},k}\rangle$ (fm^2) is shown for each level with quasiparticle energy $E_k < 3$ MeV. The number in parenthesis is the quasiparticle energy E_k (MeV). The SkM* and the surface-type pairing force are used.

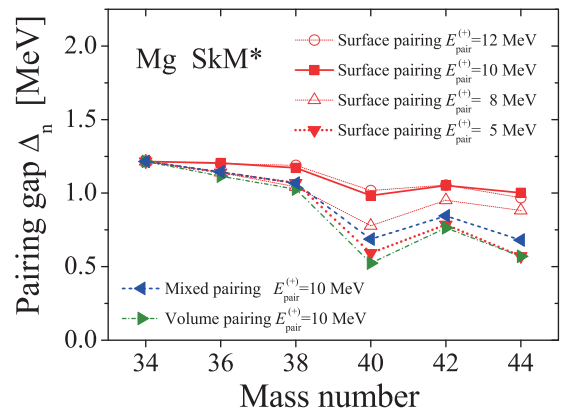

FIG. 5. Cutoff energy $E^{(+)}_{\rm pair}$ dependence of the neutron pairing gaps Δ_n. The SkM* and the surface-type pairing force are used. The results using the mixed- and volume-type pairing forces with $E^{(+)}_{\rm pair} = 10$ MeV are also compared.

about an angular correlation $\sum_m Y^*_{lm}(\hat{\mathbf{r}}_1)Y_{lm}(\hat{\mathbf{r}}_2) \sim P_l(\cos\theta_{12})$ with respect to the relative angle θ_{12} between the positions $\mathbf{r}_1$ and $\mathbf{r}_2$ of the two neutrons. Here, the Legendre polynomial $P_l(\cos\theta_{12})$ is peaked at $\theta_{12} = 0$ and always positive for $\theta_{12} \leqslant 1/l$. If we superpose them coherently over a large number of l from zero to high orbital angular momentum $l_{\max}$, the two-particle wave function may exhibit an angular correlation at small relative angles $\theta_{12} \leqslant 1/l_{\max}$. The same argument about the continuum-coupling effect can be made for neutron pairs in deformed nuclei [53].

The volume- and mixed-type pairing forces have weak continuum-coupling effect. For example, the difference between the neutron pairing gaps in ^{44}Mg obtained by using the volume-type (mixed-type) pairing force with $E^{(+)}_{\rm pair} = 5$ and 10 MeV is 0.20 MeV (0.23 MeV). Therefore, the cutoff $E^{(+)}_{\rm pair}$ dependence for these pairing forces is not shown in Fig. 5. It is also noted that the results using these pairing forces are close to that using the surface-type pairing force with $E^{(+)}_{\rm pair} = 5$ MeV.

The HFB calculations with the surface-type pairing force give almost the constant neutron pairing gaps and the quadrupole deformation $\beta_2 \approx 0.3$ from ^{34}Mg to ^{40}Mg. By taking pairing and deformation into account, the moments of inertia (MOI) $\mathscr{I}$ are considered to be almost constant except for the mass number A dependence [53]. Namely, the normalized MOI $\bar{\mathscr{I}} = \mathscr{I}/A^{5/3}$ should be nearly constant (the $A^{5/3}$ dependence is from the rigid rotor or irrotational limit [1]). This tendency is consistent with the recent observations of the first excitation energy $E_{1\rm st}$ in ^{34,36,38,40}Mg [65–68]. Actually, the $\bar{\mathscr{I}} = (3\hbar^2/E_{1\rm st})/A^{5/3}$ of ^{34}Mg and ^{40}Mg coincide within 1%. If the volume- or mixed-type pairing force is used, the $\mathscr{I}$ becomes significantly larger due to the quenching of neutron pairing correlation around ^{40}Mg [53].

V. $K^\pi = 0^+$ EXCITATIONS

A. Strength functions

Figure 6 displays the QRPA strength distributions of the $K^\pi = 0^+$ isoscalar quadrupole excitations from ^{34}Mg to the neutron drip line nucleus. The SkM* and the surface-type pairing force are used. Figure 7 is the same but the UNEDF0 is used.

As seen in Fig. 6 (Fig. 7), the first excited state in ^{34}Mg at the excitation energy $E_\nu = 1.96$ MeV (1.73 MeV) has the large transition strength $B(Q^{\rm IS}2) = 73.78$ fm^4 (89.60 fm^4). The transition strengths of the first excited states in ^{36}Mg and ^{38}Mg are small, while the first excited state in ^{40}Mg at $E_\nu = 1.84$ MeV (1.98 MeV) has the large transition strength $B(Q^{\rm IS}2) = 53.98$ fm^4 (79.98 fm^4). The large transition strengths below 2 MeV also appear in Mg isotopes with the neutron number $N \geqslant 30$.

The QRPA excitation is generated by coherent superposition of both ph- and pp-type configurations. The transition strengths without dynamical pairing effect, i.e., QRPA calculation ignoring the residual pairing interactions, are also shown in Figs. 6 and 7. It should be noted that the transition strengths of low-lying state are drastically reduced when the dynamical pairing effect is ignored.

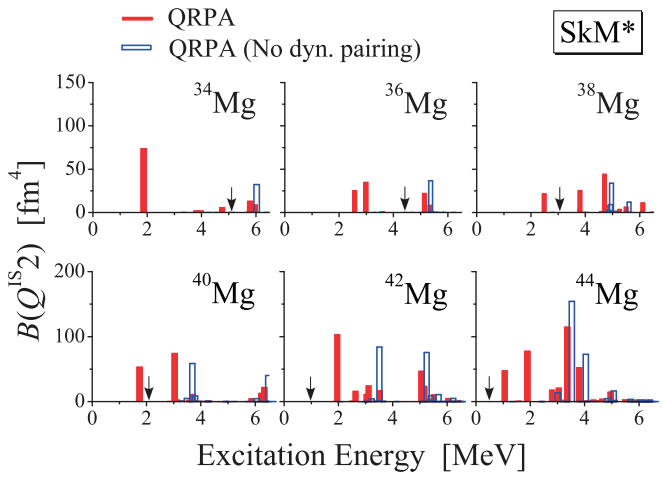

FIG. 6. QRPA strength distributions for the $K^\pi = 0^+$ isoscalar quadrupole excitations from ^{34}Mg to the neutron drip line are shown. The QRPA calculation without dynamical pairing correlation is compared. The SkM* and the surface-type pairing force with $E^{(+)}_{\rm pair} = 10$ MeV are used. The arrow indicates the neutron threshold energy.

In terms of the asymptotic quantum numbers, the nonzero ph-type matrix element

$$\langle [N'n'_z\Lambda']\Omega'|r^2Y_{20}|[Nn_z\Lambda]\Omega\rangle \neq 0 \tag{41}$$

should have $\Delta N = |N' - N| = 2$, and thus the excitation is associated with the high-frequency quadrupole mode [28]. However the pairing correlation is included, the low-lying excitation can appear by the fluctuation of pair occupation in Nilsson orbits with different spatial shapes [28–30].

According to this mechanism, the low-lying transition strengths in neutron-rich Mg isotopes can be outlined. As seen in Fig. 3, the shell gap at $N = 22$ is composed of the prolate-type orbit [321]3/2 and the oblate-type orbit [202]3/2, and the first excited state in ^{34}Mg has the large transition strength.

The prolate-type orbit [312]5/2 just above (below) the shell gap at $N = 24$ (26) has the small quadruple matrix element $\beta_k = \langle\varphi_{{\rm can},k}|r^2Y_{20}|\varphi_{{\rm can},k}\rangle$, and the transition strength below the neutron threshold energy is small in ^{36}Mg (^{38}Mg).

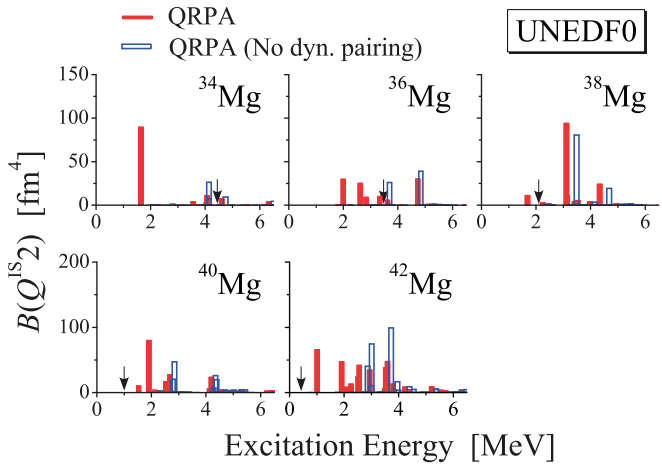

FIG. 7. Same as Fig. 6 but the UNEDF0 is used.

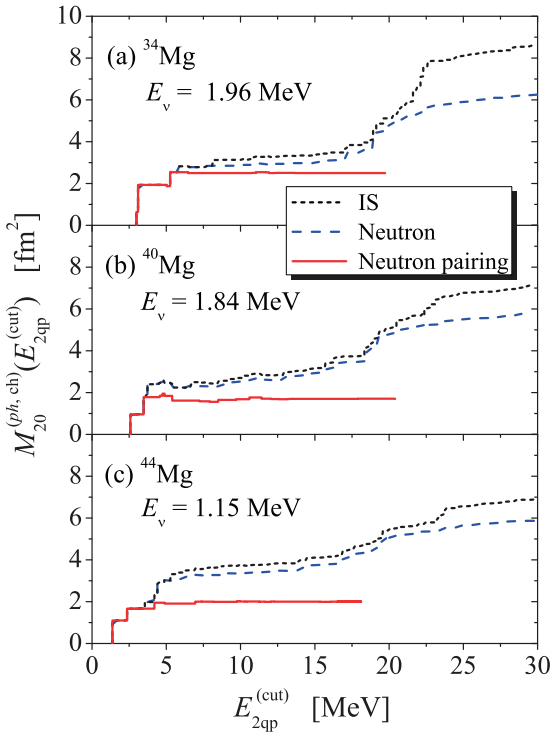

FIG. 8. Partial sum of transition matrix elements $M_{20}^{(\mathrm{ph,ch})}(E_{2\mathrm{qp}}^{(\mathrm{cut})})$ for the lowest $K^\pi = 0^+$ states in ^{34,40,44}Mg. Short dashed, dashed, and solid lines denote the isoscalar (ch = IS), neutron (ch = n), and neutron pairing [ch = n (pair)] channels. The SkM* and the surface-type pairing force are used.

On top of that, $N = 26$ is composed of prolate-type orbits only, and the low-lying transition strength is more suppressed in ^{38}Mg.

The $N = 28$ shell gap is composed of the prolate-type orbit [310]1/2 and the oblate-type orbit [303]7/2. Around the shell gaps at $N = 30$ and 32, the single-particle levels of the prolate-type [440]1/2 and [321]1/2 and the oblate-type [312]3/2 and [303]7/2 are close to each other. Eventually, the large low-lying transition strengths can appear in Mg isotopes with $N \geqslant 28$.

In the subsequent Secs. V B and V C, I focus on the microscopic structure of the lowest $K^\pi = 0^+$ states in ^{34,40,44}Mg as illustrative examples. The contribution of the pairing effect, the low-energy ph-type configurations, and the coupling to the high-frequency quadrupole mode is clarified by analyzing the partial sum of transition matrix elements $M_{20}^{(\mathrm{ph,ch})}(E_{2\mathrm{qp}}^{(\mathrm{cut})})$. I show the results using the SkM* but the same conclusion can be drawn with the UNEDF0 (see also discussion in Sec. V E).

B. ^{34}Mg

Figure 8(a) displays the partial sum of transition matrix elements $M_{20}^{(\mathrm{ph,ch})}(E_{2\mathrm{qp}}^{(\mathrm{cut})})$ for the lowest $K^\pi = 0^+$ state at $E_\nu = 1.96$ MeV in ^{34}Mg. The short dashed, dashed, and solid lines denote the isoscalar (ch = IS), neutron (ch = n), and neutron pairing [ch = n (pair)] channels. In Table I, the isoscalar transition matrix elements $M_{20}^{(\mathrm{ph,IS})}$ are classified into the neutron pairing [ch = n (pair)], neutron ph [ch = n (no pair)], and proton ph channels as percentages. One finds that the main pp-type configurations are in the low two-quasiparticle energy $E_{2\mathrm{qp}}$ (low-$E_{2\mathrm{qp}}$) part where $E_{2\mathrm{qp}}$ satisfies $0 < E_{2\mathrm{qp}} < 7.5$ MeV. The ph channel is decomposed into the low-$E_{2\mathrm{qp}}$, the middle-$E_{2\mathrm{qp}}$ (mid-$E_{2\mathrm{qp}}$, $7.5 < E_{2\mathrm{qp}} < 17.5$ MeV), and the high-$E_{2\mathrm{qp}}$ (high-$E_{2\mathrm{qp}}$, $E_{2\mathrm{qp}} > 17.5$ MeV) parts.

TABLE I. Isoscalar transition matrix elements $M_{20}^{(\mathrm{ph,IS})}$ of the lowest $K^\pi = 0^+$ states in ^{34,40,44}Mg. The breakdowns $M_{20}^{(\mathrm{ph},n(\mathrm{pair}))}$, $M_{20}^{(\mathrm{ph},n(\mathrm{no\ pair}))}$, and $M_{20}^{(\mathrm{ph},p)}$ are listed as percentages. The ph channels are decomposed into the low-$E_{2\mathrm{qp}}$, mid-$E_{2\mathrm{qp}}$, and high-$E_{2\mathrm{qp}}$ parts. The ratios of neutron to proton transition matrix elements are also shown. See text for the details.

	^{34}Mg	^{40}Mg	^{44}Mg
$M_{20}^{(\mathrm{ph,IS})}$ (fm^2)	8.59	7.34	6.89
$M_{20}^{(\mathrm{ph},n(\mathrm{pair}))}$	29.1%	23.9%	28.9%
$M_{20}^{(\mathrm{ph},n(\mathrm{no\ pair}))}$	43.7%	57.5%	56.3%
low-$E_{2\mathrm{qp}}$	3.4%	10.3%	18.6%
mid-$E_{2\mathrm{qp}}$	1.7%	2.7%	2.8%
high-$E_{2\mathrm{qp}}$	38.6%	44.5%	34.9%
$M_{20}^{(\mathrm{ph},p)}$	27.2%	18.6%	14.8%
low-$E_{2\mathrm{qp}}$	0.0%	2.2%	4.4%
mid-$E_{2\mathrm{qp}}$	4.0%	0.9%	0.8%
high-$E_{2\mathrm{qp}}$	23.2%	15.5%	9.6%
$\frac{M_{20}^{(\mathrm{ph},n)}}{M_{20}^{(\mathrm{ph},p)}} / \frac{N}{Z}$	1.46	1.87	2.17

The two-quasiparticle configurations generating the lowest $K^\pi = 0^+$ state are clearly separated into the pairing channel and the ph high-$E_{2\mathrm{qp}}$ part. The main pp-type configurations are the oblate-type pair $[202]3/2 \otimes \overline{[202]3/2}$ and the prolate-type pairs $[321]3/2 \otimes \overline{[321]3/2}$ and $[330]1/2 \otimes \overline{[330]1/2}$. Once the dynamical pairing effect is included, the high-$E_{2\mathrm{qp}}$ configurations generates the large transition strength (61.8% contribution to $M_{20}^{(\mathrm{ph,IS})}$).

C. ^{40}Mg and ^{44}Mg

Figure 8(b) displays the partial sum of transition matrix elements $M_{20}^{(\mathrm{ph,ch})}(E_{2\mathrm{qp}}^{(\mathrm{cut})})$ for the lowest $K^\pi = 0^+$ state at $E_\nu = 1.84$ MeV in ^{40}Mg, and (c) is for the $K^\pi = 0^+$ state at $E_\nu = 1.15$ MeV in ^{44}Mg.

Table I shows the breakdown of the isoscalar transition matrix elements $M_{20}^{(\mathrm{ph,IS})}$ of these states. In ^{40}Mg, the pairing channel contributes 23.9%. The main pp-type configurations are the prolate-type pairs $[310]1/2 \otimes \overline{[310]1/2}$ (13.4%) and $[440]1/2 \otimes \overline{[440]1/2}$ (−3.6%; the minus sign means the reduction of $M_{20}^{(\mathrm{ph,IS})}$), and the oblate-type pair $[303]7/2 \otimes \overline{[303]7/2}$ (11.6%). In ^{44}Mg, the pairing channel contributes 28.9%. The main pp-type configurations are the prolate-type pair $[440]1/2 \otimes \overline{[440]1/2}$ (16.0%) and the oblate-type pairs $[312]3/2 \otimes \overline{[312]3/2}$ (8.3%) and $[303]7/2 \otimes \overline{[303]7/2}$ (4.1%).

Unlike ^{34}Mg, the ph-type configurations in the low-$E_{2\mathrm{qp}}$ part can contribute around the drip line. This is due to violation of the asymptotic selection rule, Eq. (41), when weakly bound and continuum states are involved [30].

In ^{40}Mg, the neutron ph channel in the low-E_{2qp} part contributes 10.3%. The ph excitation from the weakly bound [310]1/2 state to the resonant [310]1/2 state contributes 7.6%. In ^{44}Mg, the contribution of neutron ph-type configurations in the low-E_{2qp} part is 18.6%, and this is much larger than 3.4% in ^{34}Mg and 10.3% in ^{40}Mg. In ^{44}Mg, not only the configuration from the weakly bound state [310]1/2 to the resonant state [321]1/2 (4.35%) but also configuration from the resonant state [321]1/2 to the resonant state [301]1/2 (7.83%) are involved.

Eventually, the large low-lying transition strength appears by cooperative contributions of the pairing effect, the low-energy ph configurations, and the coupling to the high-frequency quadrupole mode.

Table I also displays the ratio of neutron to proton transition matrix elements $(M_{20}^{(\mathrm{ph},n)}/M_{20}^{(\mathrm{ph},p)})/(N/Z)$. Because the neutron two-quasiparticle configurations involving weakly bound and continuum states have spatially extended structure, the low-lying excitations become neutron dominant due to the weak correlations between neutrons and protons around the neutron drip line.

D. Summation of low-lying transition strength

The influence of dineutron correlation on low-lying dipole excitations in spherical nuclei has been discussed extensively in the light-mass region [3–6] and in the medium-heavy–mass region [11,15]. In this subsection, I clarify the connection between the low-lying transition strength of $K^\pi = 0^+$ excitation and the coherent contribution of nonresonant continuum states in pairing. For this purpose, the summed transition strength up to the cutoff energy $E_{\mathrm{QRPA}}^{(\mathrm{cut})}$,

$$S_{\mathrm{IS2}}\left(E_{\mathrm{QRPA}}^{(\mathrm{cut})}\right) = \sum_{E_\nu \leqslant E_{\mathrm{QRPA}}^{(\mathrm{cut})}} B\left(Q^{\mathrm{IS}}2;\nu\right), \tag{42}$$

is examined. I adopt the cutoff energy $E_{\mathrm{QRPA}}^{(\mathrm{cut})} = 6$ MeV that covers the low-lying broad resonance in the neutron drip line nucleus (see Figs. 6 and 7). The convergence of $S_{\mathrm{IS2}}(6\ \mathrm{MeV})$ in **k**-space mesh will be checked in the Appendix.

Figure 9 shows the summed transition strengths $S_{\mathrm{IS2}}(6\ \mathrm{MeV})$ obtained with the SkM* and the surface-type pairing force. First, I consider the results of the RPA and the QRPA without dynamical pairing effect. In these calculations, the $S_{\mathrm{IS2}}(6\ \mathrm{MeV})$ increase abruptly in ^{40}Mg due to the ph-type configuration from the weakly bound state [310]1/2 to the resonant state [321]1/2. In ^{44}Mg with static pairing, due to the nonzero occupation probability of the resonant state [321]1/2, the ph excitation to the resonant state [301]1/2 enlarges the $S_{\mathrm{IS2}}(6\ \mathrm{MeV})$.

The coherent contribution of nonresonant continuum states in pairing suggests the presence of dineutron correlation [11,12,23,53]. In QRPA with dynamical pairing, the $S_{\mathrm{IS2}}(6\ \mathrm{MeV})$ converges with the pairing cutoff energy $E_{\mathrm{pair}}^{(+)} = 5$ MeV around ^{34}Mg, while the nonresonant continuum states up to $E_{\mathrm{pair}}^{(+)} = 10$ MeV contribute and enhance the $S_{\mathrm{IS2}}(6\ \mathrm{MeV})$ as it approaches the neutron drip line. This large $S_{\mathrm{IS2}}(6\ \mathrm{MeV})$ could be a good experimental probe for exploring the novel pairing correlations.

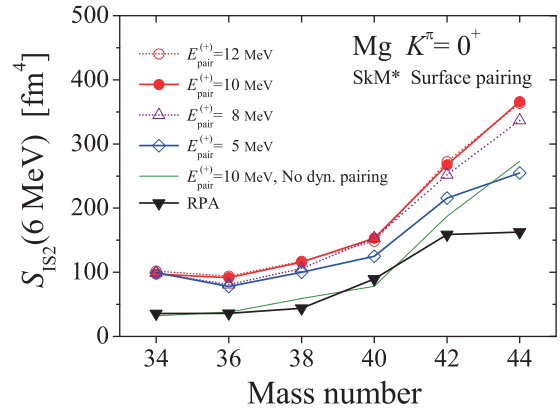

FIG. 9. Cutoff energy $E_{\mathrm{pair}}^{(+)}$ dependence of summed transition strength $S_{\mathrm{IS2}}(6\mathrm{MeV})$ for the $K^\pi = 0^+$ excitations in Mg isotopes. The SkM* and the surface-type pairing force are used. The results of the RPA and the QRPA without dynamical pairing using $E_{\mathrm{pair}}^{(+)} = 10$ MeV are also shown.

E. Interaction dependence

The summed transition strength $S_{\mathrm{IS2}}(6\ \mathrm{MeV})$ is a quantity that is sensitive to pairing properties around the neutron drip line. Similar to the neutron pairing gap, the pairing force dependence of $S_{\mathrm{IS2}}(6\ \mathrm{MeV})$ becomes sizable around the neutron drip line as shown in Fig. 10. Here, the cutoff energy $E_{\mathrm{pair}}^{(+)} = 10$ MeV is used for the volume- and mixed-type pairing forces. It should be noted that the volume- and mixed-type pairing forces have weak continuum-coupling effect, and the $S_{\mathrm{IS2}}(6\ \mathrm{MeV})$ almost coincides with that using the surface-type pairing with $E_{\mathrm{pair}}^{(+)} = 5$ MeV.

In order to quantify the influence of pairing forces on the strength distributions, the average excitation energy above the neutron threshold energy E_{th},

$$\bar{E}_{\mathrm{cont}} = \frac{\sum_{E_{\mathrm{th}} \leqslant E_\nu \leqslant 6\ \mathrm{MeV}} E_\nu\, B(Q^{\mathrm{IS}}2;\nu)}{\sum_{E_{\mathrm{th}} \leqslant E_\nu \leqslant 6\ \mathrm{MeV}} B(Q^{\mathrm{IS}}2;\nu)}, \tag{43}$$

is considered. In the same way, the average excitation energy $\bar{E}_{\mathrm{disc}}$ below the neutron threshold energy E_{th} is defined. Here,

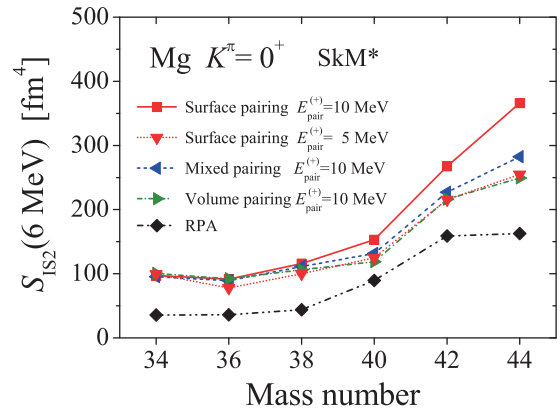

FIG. 10. Same as Fig. 9 but results using the surface-, mixed-, and volume-type pairing forces with $E_{\mathrm{pair}}^{(+)} = 10$ MeV are compared. The results of the RPA and the QRPA using the surface-type pairing with $E_{\mathrm{pair}}^{(+)} = 5$ MeV are also shown.

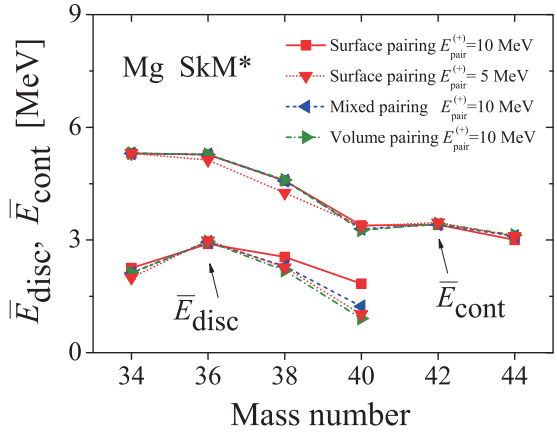

FIG. 11. Average excitation energies $\bar{E}_{\rm disc}$ and $\bar{E}_{\rm cont}$ below and above the neutron threshold energy of the QRPA strength distributions. The SkM* is used. The results using the surface-, mixed-, and volume-type pairing forces with $E_{\rm pair}^{(+)} = 10$ MeV and the surface-type pairing force with $E_{\rm pair}^{(+)} = 5$ MeV are compared.

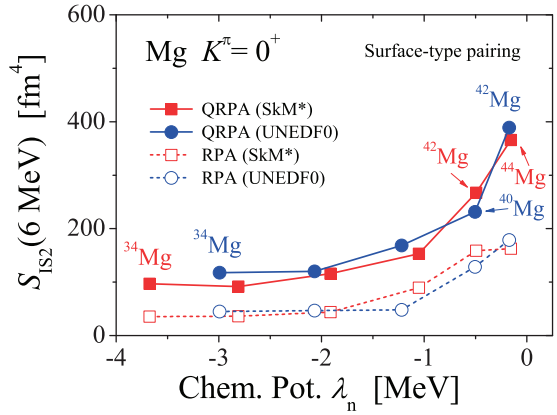

FIG. 13. Summed transition strengths $S_{\rm IS2}(6\ {\rm MeV})$ of the $K^\pi = 0^+$ excitations in Mg isotopes are shown as a function of the neutron chemical potential λ_n. The surface-type pairing force with $E_{\rm pair}^{(+)} = 10$ MeV is used for both the SkM* and the UNEDF0. The result of RPA is also shown.

the $\bar{E}_{\rm disc}$ corresponds the energy of the first excited state in the case of ^{34,38,40}Mg (except ^{40}Mg using the UNEDF0).

Figure 11 shows the average excitation energies $\bar{E}_{\rm disc}$ and $\bar{E}_{\rm cont}$. One notices that they are insensitive to the treatment of the pairing force in ^{34,36,38}Mg, because the strength distributions are almost unchanged.

On the other hand, the results of ^{40,42,44}Mg are sensitive to the treatment of the pairing force. To see this more precisely, the strength distributions in ^{40}Mg obtained by using the surface- and volume-type pairing forces with $E_{\rm pair}^{(+)} = 10$ MeV are compared in Fig. 12. The excitation energy of the first excited state goes down to $E_\nu = 0.90$ MeV and the transition strength decreases by 42.9% to $B(Q^{\rm IS}2) = 30.81$ fm^4 due to the smaller pairing correlation in calculation using the volume-type pairing force. The results using the surface-type pairing force with $E_{\rm pair}^{(+)} = 5$ MeV and the mixed-type pairing force are almost the same as that using the volume-type pairing force and are not shown here.

Compared to the summed transition strengths over the interval $E_{\rm th} \leqslant E_\nu \leqslant 6$ MeV in the calculation using the surface-type pairing force with $E_{\rm pair}^{(+)} = 10$ MeV, it is reduced by 11.2% in ^{40}Mg, 17.7% in ^{42}Mg, and 31.9% in ^{44}Mg when the volume-type pairing force is used.

Although the average excitation energy $\bar{E}_{\rm cont}$ is insensitive to the treatment of the pairing force, the resonance shape may have information about pairing properties such as dineutron correlation. For example, as shown in Fig. 12, it seems that the one broad resonance appears in ^{44}Mg when the surface-type pairing force with $E_{\rm pair}^{(+)} = 10$ MeV is used. On the other hand, one may notice the two peaks at $E_\nu \approx 1$ and 3 MeV in the case of the volume-type pairing force. This two-peak-like structure also appears in calculations using the surface-type pairing force with $E_{\rm pair}^{(+)} = 5$ MeV and the mixed-type forces. However, the resolution of the discretized-continuum strength distributions is not enough to extract a clear conclusion. I defer this analysis for future investigations, because it requires the much smaller mesh spacing Δk in **k** space or the exact treatment of the asymptotic form of wave functions in the QRPA calculation.

I expect that the discussion can hold with other EDFs. In Fig. 13, the results with the SkM* and UNEDF0 are compared. The surface-type pairing force with $E_{\rm pair}^{(+)} = 10$ MeV is used. Because of the different neutron drip lines, the $S_{\rm IS2}(6\ {\rm MeV})$ is plotted as a function of the neutron chemical potential λ_n.

One finds that the $S_{\rm IS2}(6\ {\rm MeV})$ have same tendency in spite of the different EDFs, and both the weakly bound effect and the pairing correlation due to the coupling to nonresonant continuum states enhance the $S_{\rm IS2}(6\ {\rm MeV})$ around the neutron drip line.

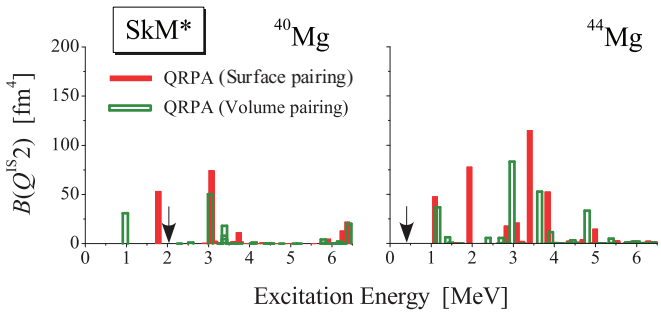

FIG. 12. QRPA strength distributions for the $K^\pi = 0^+$ isoscalar quadrupole excitations in ^{40}Mg and ^{44}Mg. The SkM* is used. The results using the surface-type and volume-type pairing forces with $E_{\rm pair}^{(+)} = 10$ MeV are compared. The arrow indicates the neutron threshold energy.

VI. CONCLUSION

In order to investigate the nature of collective excitations in weakly bound nuclei with deformation and superfluity, I have developed a new method for the QRPA calculation with the Skyrme EDF in three-dimensional wave-number space.

The wave functions with spatially extended structure in **r** space translate into a narrow distribution, and the multipole operators of the radial dependence r^L (r^2 for $L = 0$) are decreasing functions of $|\mathbf{k}|$ in **k** space. Eventually, the dominant contribution to the ph-type matrix element comes from the low-$|\mathbf{k}|$ region, and the QRPA calculation requires much smaller mesh space than that in **r**-space mesh. This advantage allows one to perform the QRPA calculation without assuming axial symmetry and time-reversal symmetry on wave functions by using a single-core CPU with 3.5 GB memory. The QRPA code can be applied to various collective dynamics in unstable nuclei; for example, rotating nuclei [80] and the microscopic construction of the collective Hamiltonian based on the local QRPA approach [81].

I discussed the role of continuum states for pairing correlation in neutron-rich Mg isotopes. The coherent contribution of nonresonant continuum states up to $E^{(+)}_{\rm pair} = 10$ MeV is sizable around the drip line when the surface-type pairing force is used. This suggest the presence of dineutron correlation [11,15,53]. On the other hand, the continuum effect is weak with the volume- and mixed-type pairing forces, and the neutron pairing gap decreases as it approaches the neutron drip line.

The Skyrme HFB calculation with the surface-type pairing force gives almost constant neutron pairing gaps and quadrupole deformations $\beta_2 \approx 0.3$ from ^{34}Mg to ^{40}Mg. This is consistent with the recent observations of the first excitation energies in ^{34,36,38,40}Mg [65–68], that suggest the nearly constant normalized MOI $\bar{\mathscr{I}} = \mathscr{I}/A^{5/3}$ [53].

I also clarified the pairing effect on the $K^\pi = 0^+$ isoscalar quadrupole excitation in neutron-rich Mg isotopes. The dynamical pairing correlation plays the essential role for the existence of low-lying $K^\pi = 0^+$ excitations. The cooperative role of the pairing correlation and the low-energy ph configurations involving weakly bound and continuum states is discussed. Especially, I emphasized that the coherent contribution of nonresonant continuum states in pairing enhances the low-lying strengths around the neutron drip line. This fact could be a good experimental probe to explore the novel pairing properties such as dineutron correlation.

ACKNOWLEDGMENTS

I am grateful to K. Matsuyanagi, H. Sagawa, K. Hagino, M. Matsuo, T. Nakatsukasa, and K. Yoshida for valuable discussions. Numerical computation in this work was carried out on the supercomputer CRAY XC40 at the Yukawa Institute Computer Facility in Kyoto University.

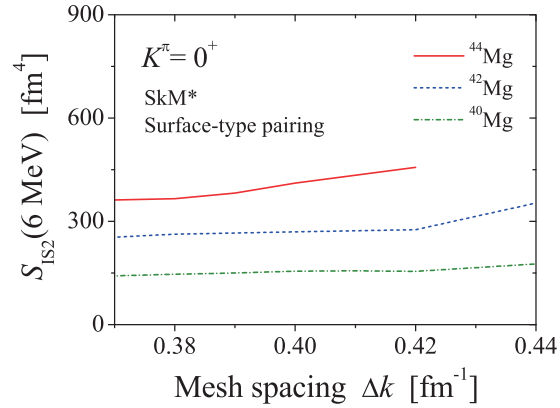

FIG. 14. Summed transition strengths $S_{\rm IS2}$(6 MeV) in ^{34,42,44}Mg as a function of Δk. The SkM* and the surface-type pairing force with $E^{(+)}_{\rm pair} = 10$ MeV are used. The $N_{\rm max} = 12$ is fixed.

APPENDIX: CONVERGENCE IN k SPACE

The ph excitations involving the spatially extended wave functions such as halo states require the accurate description of the low density region outside the nuclear surface in **r** space. For example, the up-to-date QRPA in the axially symmetric **r**-space mesh used the large box size $R_{\rm b} = 27.6$ fm and the mesh spacing 0.6 fm (46 grid points for both z and r axis directions) for description of the pygmy dipole excitations in ^{40}Mg [38]. If it is directly extended to the three-dimensional **r**-space mesh with parity and signature symmetries, the estimated number of mesh points is about $(46)^3 = 97336$.

In marked contrast to the **r**-space mesh, the main contribution to the ph-type matrix elements $O_{LK,kk'}$ comes from low-$|\mathbf{k}|$ region in **k**-space mesh (see discussion in Secs. III B and V A). In my calculations, the model space parameters $N_{\rm max} = 12$ and $\Delta k = 0.38$ fm^{-1} for $k_{\rm max} = 4.56$ fm^{-1} are adopted. If the $N_{\rm max}$ increases to 13, for example, the summed transition strength $S_{\rm IS2}$(6 MeV) in ^{44}Mg changes 0.21% in the calculation using the SkM* and the surface-type pairing force.

The mesh spacing Δk should be chosen carefully for description of wave functions in the low-$|\mathbf{k}|$ region. In Fig. 14, the summed transition strengths $S_{\rm IS2}$(6 MeV) in ^{40,42,44}Mg are shown as a function of Δk. Here, ^{44}Mg is unbound for $\Delta k > 0.42$ fm^{-1}. One notices that the $\Delta k = 0.38$ fm^{-1} gives a reasonable result even for the neutron drip line nucleus ^{44}Mg. The number of mesh points is 455 for $N_{\rm max} = 12$ and $\Delta k = 0.38$ fm^{-1}. This number is 214 times smaller than the number of mesh points in **r** space.

[1] P. Ring and P. Schuck, *The Nuclear Many-body Problem* (Springer-Verlag, Berlin, 1980).
[2] D. M. Brink and R. A. Broglia, *Nuclear Superfluidity: Pairing in Finite Systems* (Cambridge University Press, Cambridge, 2005).
[3] G. F. Bertsch and H. Esbensen, Ann. Phys. (NY) **209**, 327 (1991).
[4] K. Hagino and H. Sagawa, Phys. Rev. C **72**, 044321 (2005).
[5] T. Myo, Y. Kikuchi, K. Katō, and K. Ikeda, Prog. Theor. Phys. **119**, 561 (2008).
[6] T. Nakamura *et al.*, Phys. Rev. Lett. **96**, 252502 (2006).
[7] K. Ikeda, Nucl. Phys. A **538**, 355c (1992).
[8] M. V. Zhukov, B. V. Danilin, D. V. Fedorov, J. M. Bang, I. J. Thompson, and J. S. Vaagen, Phys. Rep. **231**, 151 (1993).
[9] S. Aoyama, T. Myo, K. Katō, and K. Ikeda, Prog. Theor. Phys. **116**, 1 (2006).
[10] Y. Kanada-En'yo, Phys. Rev. C **76**, 044323 (2007).
[11] M. Matsuo, K. Mizuyama, and Y. Serizawa, Phys. Rev. C **71**, 064326 (2005).

[12] M. Matsuo and T. Nakatsukasa, J. Phys. G: Nucl. Part. Phys. **37**, 064017 (2010).
[13] N. Pillet, N. Sandulescu, and P. Schuck, Phys. Rev. C **76**, 024310 (2007).
[14] N. Pillet, N. Sandulescu, P. Schuck, and J.-F. Berger, Phys. Rev. C **81**, 034307 (2010).
[15] Y. Serizawa and M. Matsuo, Prog. Theor. Phys. **121**, 97 (2009).
[16] I. Tanihata *et al.*, Phys. Rev. Lett. **100**, 192502 (2008).
[17] A. Chatterjee *et al.*, Phys. Rev. Lett. **101**, 032701 (2008).
[18] A. Lemasson *et al.*, Phys. Lett. B **697**, 454 (2011).
[19] E. Khan, N. Sandulescu, N. V. Giai, and M. Grasso, Phys. Rev. C **69**, 014314 (2004).
[20] B. Avez, C. Simenel, and Ph. Chomaz, Phys. Rev. C **78**, 044318 (2008).
[21] E. Khan, M. Grasso, and J. Margueron, Phys. Rev. C **80**, 044328 (2009).
[22] M. Matsuo and Y. Serizawa, Phys. Rev. C **82**, 024318 (2010).
[23] H. Shimoyama and M. Matsuo, Phys. Rev. C **84**, 044317 (2011).
[24] G. Potel, F. Barranco, F. Marini, A. Idini, E. Vigezzi, and R. A. Broglia, Phys. Rev. Lett. **107**, 092501 (2011); **108**, 069904(E) (2012).
[25] M. Grasso, D. Lacroix, and A. Vitturi, Phys. Rev. C **85**, 034317 (2012).
[26] G. Potel, A. Idini, F. Barranco, E. Vigezzi, and R. A. Broglia, Phys. Rev. C **87**, 054321 (2013).
[27] H. Shimoyama and M. Matsuo, Phys. Rev. C **88**, 054308 (2013).
[28] A. Bohr and B. R. Mottelson, *Nuclear Structure*, Vol. II (W. A. Benjamin, New York, 1975).
[29] K. Yoshida and M. Yamagami, Phys. Rev. C **77**, 044312 (2008).
[30] K. Yoshida, M. Yamagami, and K. Matsuyanagi, Nucl. Phys. A **779**, 99 (2006).
[31] P. Bonche, H. Flocard, P. H. Heenen, S. J. Krieger, and M. S. Weiss, Nucl. Phys. A **443**, 39 (1985).
[32] K. Yoshida and N. V. Giai, Phys. Rev. C **78**, 064316 (2008).
[33] K. Yoshida, Phys. Rev. C **80**, 044324 (2009).
[34] J. Terasaki and J. Engel, Phys. Rev. C **82**, 034326 (2010).
[35] J. Terasaki and J. Engel, Phys. Rev. C **84**, 014332 (2011).
[36] T. Nakatsukasa, T. Inakura, and K. Yabana, Phys. Rev. C **76**, 024318 (2007).
[37] K. Washiyama and T. Nakatsukasa, Phys. Rev. C **96**, 041304(R) (2017).
[38] K. Wang, M. Kortelainen, and J. C. Pei, Phys. Rev. C **96**, 031301(R) (2017).
[39] P. G. Hansen, Phys. Rev. Lett. **77**, 1016 (1996).
[40] A. L. Goodman, Adv. Nucl. Phys. **11**, 263 (1979).
[41] B. Gall, P. Bonche, J. Dobaczewski, H. Flocard, and P.-H. Heenen, Z. Phys. A **348**, 183 (1994).
[42] H. Ogasawara, K. Yoshida, M. Yamagami, S. Mizutori, and K. Matsuyanagi, Prog. Theor. Phys. **121**, 357 (2009).
[43] M. Yamagami and K. Matsuyanagi, JPS Conf. Proc. **6**, 030051 (2015).
[44] P. Bonche, H. Flocard, and P.-H. Heenen, Nucl. Phys. A **467**, 115 (1987).
[45] J. Dobaczewski, W. Nazarewicz, T. R. Werner, J. F. Berger, C. R. Chinn, and J. Dechargé, Phys. Rev. C **53**, 2809 (1996).
[46] M. Bender, P.-H. Heenen, and P.-G. Reinhard, Rev. Mod. Phys. **75**, 121 (2003).
[47] H. Esbensen, G. F. Bertsch, and K. Hencken, Phys. Rev. C **56**, 3054 (1997).
[48] J. Dobaczewski, W. Nazarewicz, and P.-G. Reinhard, Nucl. Phys. A **693**, 361 (2001).
[49] J. Dobaczewski and W. Nazarewicz, Prog. Theor. Phys. Suppl. **146**, 70 (2002).
[50] J. Margueron, H. Sagawa, and K. Hagino, Phys. Rev. C **76**, 064316 (2007).
[51] M. Matsuo, Phys. Rev. C **73**, 044309 (2006).
[52] M. Yamagami, J. Margueron, H. Sagawa, and K. Hagino, Phys. Rev. C **86**, 034333 (2012).
[53] M. Yamagami and Y. R. Shimizu, Phys. Rev. C **77**, 064319 (2008).
[54] J. Terasaki, P.-H. Heenen, H. Flocard, and P. Bonche, Nucl. Phys. A **600**, 371 (1996).
[55] P.-G. Reinhard, M. Bender, K. Rutz, and J. A. Maruhn, Z. Phys. A **358**, 277 (1997).
[56] N. Tajima, Phys. Rev. C **69**, 034305 (2004).
[57] M. Bender, K. Rutz, P.-G. Reinhard, and J. A. Maruhn, Eur. Phys. J. A **8**, 59 (2000).
[58] M. Yamagami, K. Matsuyanagi, and M. Matsuo, Nucl. Phys. A **693**, 579 (2001).
[59] H. Ogasawara, K. Yoshida, M. Yamagami, S. Mizutori, and K. Matsuyanagi, Prog. Theor. Phys. **120**, 1169 (2008).
[60] H. Sagawa, N. Van Giai, N. Takigawa, M. Ishihara, and K. Yazaki, Z. Phys. A **351**, 383 (1995).
[61] H. Oba and M. Matsuo, Phys. Rev. C **80**, 024301 (2009).
[62] S. O. Bäckman, A. D. Jackson, and J. Speth, Phys. Lett. B **56**, 209 (1975).
[63] N. Van Giai and H. Sagawa, Phys. Lett. B **106**, 379 (1981).
[64] N. Van Giai, Ch. Stoyanov, and V. V. Voronov, Phys. Rev. C **57**, 1204 (1998).
[65] K. Yoneda *et al.*, Phys. Lett. B **499**, 233 (2001).
[66] S. Takeuchi *et al.*, Phys. Rev. C **79**, 054319 (2009).
[67] P. Doornenbal *et al.*, Phys. Rev. Lett. **111**, 212502 (2013).
[68] H. L. Crawford *et al.*, Phys. Rev. Lett. **122**, 052501 (2019).
[69] R. Rodrìguez-Guzmán, J. L. Egido, and L. M. Robledo, Nucl. Phys. A **709**, 201 (2002).
[70] H. Nakada and K. Takayama, Phys. Rev. C **98**, 011301(R) (2018).
[71] S. Goriely, N. Chamel, and J. M. Pearson, Phys. Rev. C **88**, 024308 (2013).
[72] M. Kimura, T. Suhara, and Y. Kanada-Enyo, Eur. Phys. J. A **52**, 373 (2016).
[73] L. Li, J. Meng, P. Ring, E.-G. Zhao, and S.-G. Zhou, Phys. Rev. C **85**, 024312 (2012).
[74] Q. Zhi and Z. Ren, Phys. Lett. B **638**, 166 (2006).
[75] J. C. Pei, W. Nazarewicz, and M. Stoitsov, Eur. Phys. J. A **42**, 595 (2009).
[76] J. Bartel, P. Quentin, M. Brack, C. Guet, and H.-B. Håkansson, Nucl. Phys. A **386**, 79 (1982).
[77] M. Kortelainen, T. Lesinski, J. Moré, W. Nazarewicz, J. Sarich, N. Schunck, M. V. Stoitsov, and S. Wild, Phys. Rev. C **82**, 024313 (2010).
[78] W. Satula, J. Dobaczewski, and W. Nazarewicz, Phys. Rev. Lett. **81**, 3599 (1998).
[79] K. Hagino, H. Sagawa, J. Carbonell, and P. Schuck, Phys. Rev. Lett. **99**, 022506 (2007).
[80] T. Nakatsukasa, K. Matsuyanagi, M. Matsuzaki, and Y. R. Shimizu, Phys. Scr. **91**, 073008 (2016).
[81] K. Matsuyanagi, M. Matsuo, T. Nakatsukasa, K. Yoshida, N. Hinohara, and K. Sato, Phys. Scr. **91**, 063014 (2016).